Methane Oxidation Mechanism on Pt(111): A Cluster Model DFT Study

George Psofogiannakis,[*,†,#] **Alain St-Amant,**[‡] **and Marten Ternan**[†,§,#]

*Department of Chemical Engineering and Department of Chemistry, University of Ottawa,
Ottawa, Ontario, K1N 6N5, Canada, Centre for Catalysis Research and Innovation, University of Ottawa,
Ontario, K1N 6N5, Canada, and EnPross Inc., 147 Banning Road, Ottawa, Ontario, K2L 1C5, Canada*

Received: March 14, 2006; In Final Form: September 19, 2006

The electronic energy barriers of surface reactions pertaining to the mechanism of the electrooxidation of methane on Pt (111) were estimated with density functional theory calculations on a 10-atom Pt cluster, using both the B3LYP and PW91 functionals. Optimizations of initial and transition states were performed for elementary steps that involve the conversion of CH_4 to adsorbed CO at the Pt/vacuum interface. As a first approximation we do not include electrolyte effects in our model. The reactions include the dissociative chemisorption of CH_4 on Pt, dehydrogenation reactions of adsorbed intermediates ($*CH_x \rightarrow *CH_{x-1} + *H$ and $*CH_xO \rightarrow *CH_{x-1}O + *H$), and oxygenation reactions of adsorbed CH_x species ($*CH_x + *OH \rightarrow *CH_x\text{-}OH$). Many pathways were investigated and it was found that the main reaction pathway is $CH_4 \rightarrow *CH_3 \rightarrow *CH_2 \rightarrow *CH \rightarrow *CHOH \rightarrow *CHO \rightarrow *CO$. Frequency analysis and transition-state theory were employed to show that the methane chemisorption elementary step is rate-limiting in the above mechanism. This conclusion is in agreement with published experimental electrochemical studies of methane oxidation on platinum catalysts that have shown the absence of an organic adlayer at electrode potentials that allow the oxidation of adsorbed CO. The mechanism of the electrooxidation of methane on Pt is discussed.

Introduction

The electrooxidation of methane in low-temperature fuel cells is a slow process that has received little attention by the scientific community in recent years. Nevertheless, the direct oxidation of methane at low temperatures (60–150 °C) has been experimentally demonstrated by several workers on various types of platinum anode electrodes with use of acid electrolytes, such as phosphoric acid,[1] hydrofluoric acid,[2] sulfuric acid,[3–6] and perchloric acid,[7,8] as well as polymer electrolyte membranes.[9,10] The thermodynamic efficiency limit for complete methane oxidation to CO_2 in a CH_4/O_2 fuel cell at 25 °C is[11] 92%. However, the process is of limited technical interest because of very slow anode kinetics. Among saturated hydrocarbons, methane has the smallest rate of electrooxidation.[12] In all experiments that the CO_2 yield has been measured,[1–3,6] it was found that it is very close to ~100% and no other products have been reported.

The rate of adsorption of methane from $HClO_4$ electrolyte on Teflon-bonded Pt electrodes has been previously investigated[7] with potentiodynamic electrochemical methods. In these experiments, methane was allowed to adsorb on the electrocatalyst for several different periods of time at electrode potentials in the range 0.2–0.6 V vs RHE. The adlayer was then oxidized with an anodic potential sweep and the charge that passed through the interface, which indicates the amount of adsorbed material, was measured. It was found that the maximum rate of adsorption occurs at adsorption potentials around 0.3 V and that for adsorption potentials greater than about 0.45 V, the

surface coverage after long adsorption times is very small. The authors noted that at these intermediate potentials, the rate of oxidation of the adlayer is increased, and the adsorption process becomes rate limiting. In another study,[5] similar electrochemical methods were used to arrive at the conclusion that methane chemisorption on Pt in H_2SO_4 becomes rate limiting at potentials of ~0.3 V. At higher potentials the reaction proceeds on a surface that is free of any adsorbed carbon-containing species.

For adsorption at potentials in the hydrogen region (0–0.35 V), CO and other adsorbates can be present on the surface. The presence of a carbon-containing adsorbate in an oxidized state was first inferred indirectly from electrochemical experiments.[13] In situ infrared spectroscopy was later used[14] to investigate the mechanism of CH_4 electrooxidation at 25 °C in $HClO_4$ on noble metal electrodes. After adsorption at 0.26 V on Pt, the presence of *CO and *CHO (or *COOH) on the Pt surface was detected (the asterisk refers to an adsorbed species). The presence of *CO is not surprising. It is the major surface species in the oxidation of all carbon-containing molecules that have been investigated, including methanol, formic acid, formaldehyde, and H_2/CO mixtures. It acts as either a surface blocking species or a reactive intermediate or both. Adsorbed CO at the metal–solution interface is oxidized at intermediate electrode potentials presumably by surface hydroxyl (OH) groups.[15,16]

The overall anode reaction that takes place during methane electrooxidation can be written as:

$$CH_4 + 2H_2O \rightarrow CO_2 + 8H^+ + 8e^- \qquad (1)$$
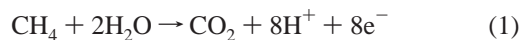
Bagotzky et al.[17] have proposed a generalized reaction network of the possible elementary steps involved in the mechanism of electrooxidation of methane and other C_1 organics. For methane this network is shown in Figure 1, in which we have excluded the formation of other stable molecules (CH_3OH, H_2CO, and

* Address correspondence to this author. E-mail: psofogi@hotmail.com. Phone: (+1) 613-562-5800 ext. 6120.
† Department of Chemical Engineering, University of Ottawa.
# Centre for Catalysis Research and Innovation.
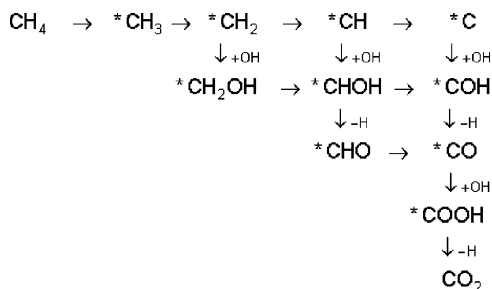‡ Department of Chemistry, University of Ottawa.
§ EnPross Inc.

$$CH_4 \rightarrow {}^*CH_3 \rightarrow {}^*CH_2 \rightarrow {}^*CH \rightarrow {}^*C$$
$$\downarrow {+OH} \quad\quad \downarrow {+OH} \quad\quad \downarrow {+OH}$$
$${}^*CH_2OH \rightarrow {}^*CHOH \rightarrow {}^*COH$$
$$\downarrow {-H} \quad\quad \downarrow {-H}$$
$${}^*CHO \rightarrow {}^*CO$$
$$\downarrow {+OH}$$
$${}^*COOH$$
$$\downarrow {-H}$$
$$CO_2$$

Figure 1. The Bagotzky mechanism for the electrooxidation of methane.

HCOOH) based on the experimental observation of 100% CO_2 yield on platinum. The various suggestions for the rate-limiting step have included methane adsorption[7] as noted above, dehydrogenation of adsorbed unspecified hydrocarbon intermediates,[5] and dehydrogenation of adsorbed CH_3 intermediates[6] following methane adsorption.

Unlike at the electrochemical interface, the chemisorption of methane at the metal−gas interface has been the focus of several studies because of its relevance to industrially important catalytic reactions, particularly steam reforming.[18] Single-crystal surfaces of platinum and various other metals have been studied. In steam reforming of methane the C−H bond cleavage of the very stable methane molecule is the rate-limiting step.[18−20] Most of the experimental studies are molecular beam studies[21−28] that independently assess the effects of translational and vibrational energies of the beam, the surface temperature, and the angle of incidence. Theoretical models have also been proposed.[20,29,30] The mechanism of the chemisorption process of methane has not been unequivocally verified.[20,22,26,27,31] Direct dissociation,[23,28,30,31] steering-assisted direct dissociation,[21] precursor-mediated dissociation,[26,29] and quantum mechanical tunneling[20] are some of the mechanisms that have been proposed to explain experimental trends of the sticking probability data from methane molecular beams. Other complications arise because the translational energies used in molecular beams are much higher than catalytic reactors and because it is usually not possible to predict the outcome of thermal activation experiments from the results of molecular beam results.[18,22] Perhaps more relevant to fuel cell conditions is a low-temperature thermal "bulb" experimental study,[31] in which methane dissociation on Pt(110) was interpreted by a direct dissociation mechanism. The evidence for direct dissociation is stronger than precursor-mediated dissociation[18,21,23] because it can explain the observed large increase in CH_4 sticking probability with increasing kinetic energy of the beam. Dynamic steering[32] in a direct dissociation mechanism has been used[21] to explain the observed minimum in the CH_4 sticking probability at low translational energies.

Our objective in this study is to use quantum-mechanical methodology to predict the mechanism and rate-determining step of the anodic methane oxidation reaction on a Pt(111) surface. This may result in understanding the requirements and attributes of a possible improved catalyst for methane electrooxidation. Several DFT studies have been directed toward mechanistic understanding of various electrochemical and fuel cell reactions.[33] No computational or theoretical studies directed toward understanding of the electrooxidation of methane have been previously reported in the literature. Also, we do not know of any study that has reported any information on the structure-sensitivity of the methane electrooxidation reaction. Thus, as a first step we have chosen to limit our scope to the Pt(111) surface.

Despite considerable advances in computational methodologies, the currently available "ab initio" computational tools do not allow the quantitative estimation of electrochemical reaction rates, particularly for complex reactions such as the one shown in eq 1. In comparison to the metal−gas interface, the electrochemical interface presents several complexities including the electrical potential field, the double-layer, the existence of a liquid phase adjacent to the metal, and the occurrence of electron-transfer reactions. These complexities are coupled with the fact that predictions of reaction rates are very sensitive to the accuracy of estimating energy barriers for surface reactions. However, DFT can be more effectively used for mechanistic studies, as well as for qualitative trends of reaction rates, such as comparing the activities of different catalysts for the same reacting system, or comparing the rates of different reactions on the same catalyst.

To predict the reaction mechanism, we estimated with DFT calculations the electronic energy barriers for the reactions shown in Figure 1, excluding the CO oxidation reaction. This general reaction network corresponds to methane oxidation reactions at the electrochemical interface but the calculation setup is the metal−vacuum interface. The absence of electrolyte in our model is an approximation that allows us to focus on metal−adsorbate interactions. The oxidant of the adsorbed CH_x radicals in the mechanism of Figure 1 was taken to be adsorbed hydroxyl radicals (OH) in analogy with the predominant view that OH is also the species that oxidizes adsorbed CO, either when CO is contained in the feed[15] or when it forms on the surface during the oxidation of organics, such as methanol.[16] The nature of the oxidizing agent in acid fuel cells has been the topic of long-standing debate. In situ X-ray scattering results[15] were interpreted in favor of reversible OH formation on Pt(111). Thus, our calculations pertain to electrode potentials greater than ∼0.4 V vs RHE in the double layer region, for which hydroxyl groups form on the Pt surface by the deprotonation of water molecules. In this range of potentials the reverse of the dehydrogenation reactions shown in Figure 1 need not be considered because the coverage of the surface with hydrogen atoms is negligible. We refrain from describing the reaction of the electrooxidation of adsorbed CO because of the well-known failure of DFT methods in predicting the most stable surface site of CO adsorption on platinum.[34] To predict the rate-limiting step, we employed transition-state theory to estimate the rate constants for some of the elementary steps, as will be described later. Based on previous work discussed above, we used direct dissociative chemisorption of methane to estimate the preexponential factor for this elementary step.

Computational and Theoretical Methods

We used a planar 10-atom Pt cluster to simulate the surface. The cluster is shown in the figures of the results section. The locations of the atoms correspond to the Pt(111) surface. This is the minimum size required to keep the optimized structures of the initial and final states of the reactions inside the boundary defined by the edge atoms of the cluster, without imposing any geometric constraints. Our objective requires the correct prediction of the relative magnitudes of the energy barriers of the elementary steps rather than chemical accuracy in their actual values. This justifies the small cluster size. However, we also support our conclusions by presenting comparisons of our results with periodic boundary condition (PBC) calculations for those elementary steps for which PBC predictions have been found in the literature. Furthermore, to investigate cluster-size effects, one calculation for a single elementary reaction was also

Methane Oxidation Mechanism on Pt(111)

J. Phys. Chem. B, Vol. 110, No. 48, 2006 **24595**

performed on a 3-layer 25-atom platinum cluster, as described in the results section.

Density functional theory (DFT) calculations were carried out with the Gaussian 03 program.[35] We used two different exchange-correlation functionals: B3LYP[36] and PW91PW91.[37] We present results for both functionals. For the Pt atoms, we used the Los Alamos National Laboratory[38] basis set of double-ζ quality (LANL2DZ) and the corresponding scalar relativistic effective core potential that replaces the inner-shell electrons. Eighteen electrons in the outer shells $5s^2 5p^6 5d^9 6s^1$ were treated explicitly. The 6-31G** basis set was used for carbon, hydrogen, and oxygen atoms. No significant spin contamination was found. For geometry optimizations, the convergence criteria corresponded to a maximum step size of 0.01 au and an RMS force of 0.0017 au. The Pt–Pt interatomic distance was kept fixed in the optimizations at the experimental bulk value,[39] 2.775 Å. No further constraints were imposed in geometry optimizations. For each adsorbate, the most stable adsorption site was found by optimizations of different starting structures, at on-top, bridged, and 3-fold hollow adsorption sites of the cluster. For most reactions the transition state (TS) was located by analytical methods as implemented in the default Gaussian 03 method. Vibrational frequency calculations were performed on all transition states at the DFT-optimized geometries with the default Gaussian03 algorithm that calculates force constants analytically. It was verified that the TS geometry possesses only one negative imaginary frequency. Animation of the TS negative frequencies allowed us to verify that the TSs corresponded to the reactions that were studied. Reaction coordinate scans were performed for all reactions by selecting an internal coordinate (a bond distance) and performing constrained energy minimizations for various fixed values of this coordinate. For the PW91 calculations the TS energy was estimated as the maximum energy of the reaction scan.

Furthermore, we investigated the effect of the spin state of the cluster–adsorbate systems. In each case, the ground state of the reactants was found by performing calculations for several different spin multiplicities (SM = 1 + number of unpaired electrons). Reaction paths were followed for the ground-state spin of the initial state for each reaction. The product state of the reaction has, in most cases, a different spin state than the reactant. We performed calculations on the reaction pathways with two and more different spin multiplicities. We observed that in every case the spin multiplicity of minimum energy did not change from the initial reactant state to the transition state. Because we are interested only in the part of the pathway up to the transition state, we present here only calculations with the minimum-energy reactant spin states. The effect of the spin state on the electronic energy of small Pt clusters has been previously examined,[40] and the preferred high-spin states were explained by a model that predicts the bonding orbitals within the cluster.

The binding energy of each of the intermediate species involved in the reaction mechanism of Figure 1 was calculated as:[41]

$$E_{\text{binding}} = E_{\text{cluster+adsorbate}} - E_{\text{cluster}} - E_{\text{adsorbate}} \quad (2)$$

where $E_{\text{cluster+adsorbate}}$, E_{cluster}, and $E_{\text{adsorbate}}$ are the total electronic energies of the optimized structures of the adsorbed configuration, the isolated bare cluster, and the isolated radical, respectively. The electronic energy barrier (non-ZPE corrected) for each reaction was calculated as the difference between the electronic energies of the transition state (TS) and initial state (IS) of the reaction:

$$\Delta E^{\ddagger}_{\text{elec}} = E^{\text{TS}}_{\text{elec}} - E^{\text{IS}}_{\text{elec}} \quad (3)$$

Within the framework of transition state theory, rate constants for adsorption and surface reaction elementary steps at the metal–vacuum interface can be estimated provided that estimates of the electronic energy barriers and the vibrational frequencies of the initial states and the transition states exist. We describe the methodology here because it was used to identify the rate-limiting step as described in the next section. The rate constant of a chemical reaction is given by:[42a]

$$k = \frac{k_{\text{B}}T}{h} \exp\left(\frac{\Delta S^{\text{o}\ddagger}}{k_{\text{B}}}\right) \exp\left(-\frac{\Delta H^{\text{o}\ddagger}}{k_{\text{B}}T}\right) \quad (4)$$

where k_{B} is Boltzmann's constant, h is Planck's constant, and $\Delta S^{\text{o}\ddagger}$ and $\Delta H^{\text{o}\ddagger}$ are the standard-state entropy and enthalpy of activation for the reaction.

A nonlinear molecule such as CH_4 has three translational, three rotational, and $3N - 6$ vibrational degrees of freedom in the gas phase, where N is the number of atoms in the molecule. In the adsorbed state, all translational and rotational degrees of freedom are replaced by vibrational modes corresponding to frustrated rotation and translation on the surface. An adsorbed molecule has $3N$ vibrational degrees of freedom. At the transition state, the mode that corresponds to the reaction coordinate gives rise to an imaginary negative frequency, and is excluded from the calculation of the partition function of the TS.[43] As a result, the calculation of the entropy of the transition state is based on $3N - 1$ vibrational modes.

For the calculation of the rate constants for these reactions we make use of eq 4. The analysis is based on statistical thermodynamics.[42b] The following equations include translational and rotational energies and entropies, which were used for gaseous methane but were not used for adsorbed intermediates. The standard enthalpy of activation for a surface reaction is approximately equal to the standard internal energy of activation and is given by:

$$\Delta H^{\text{o}\ddagger} \approx \Delta U^{\text{o}\ddagger} = \Delta U^{\text{o}\ddagger}_{\text{trans}} + \Delta U^{\text{o}\ddagger}_{\text{rot}} + \Delta U^{\text{o}\ddagger}_{\text{vib}} + \Delta(\text{ZPE}) + \\ \Delta E^{\ddagger}_{\text{el}} \quad (5)$$

where the terms on the right-hand side denote the differences in translational energy, rotational energy, vibrational thermal energy, zero-point energy, and electronic energy between the TS and the IS, respectively. The standard-state energies are evaluated for $T = 298$ K and are given by:[42b]

$$U_{\text{trans}} = \frac{3}{2}k_{\text{B}}T \quad (6)$$

$$U_{\text{rot}} = \frac{3}{2}k_{\text{B}}T \quad (7)$$

$$U_{\text{vib}} = \sum_i \frac{h\nu_i}{(e^{h\nu_i/k_{\text{B}}T} - 1)} \quad (8)$$

$$\text{ZPE} = \sum_i \frac{h\nu_i}{2} \quad (9)$$

where ν_i are the vibrational frequencies (Hz), E_{el} is the electronic energy predicted by the DFT calculation, and all quantities are evaluated on a molecular basis (J/molecule). The standard entropy of activation is given by:

$$\Delta S^{\text{o}\ddagger} = \Delta S^{\text{o}\ddagger}_{\text{trans}} + \Delta S^{\text{o}\ddagger}_{\text{rot}} + \Delta S^{\text{o}\ddagger}_{\text{vib}} \quad (10)$$

TABLE 1: Binding Energies and Binding Sites for Species in the Network of Figure 1 Predicted with B3LYP and PW91 Functionals

species	binding site	$E_{binding}$ (eV)			
		Pt$_{10}$/B3LYP (this work)	Pt$_{10}$/PW91 (this work)	Pt$_x$/B3LYP (previous work)	PBC/PW91 (previous work)
H	top	−3.02	−2.86	−2.92[a]	−2.71[b]
OH	bridge	−1.81	−2.06	−1.77[a]	−2.12[b]
CH$_3$	top	−2.17	−2.40	−2.33,[c] −2.16[d]	−1.93,[b] 2.04[e]
CH$_2$	bridge	−4.21	−4.56	−4.52,[c] −4.13[d]	−3.95[e]
CH	hollow	−7.03	−7.55	−7.22,[c] −6.36[d]	−6.43[e]
C	hollow	−6.33	−6.99	−6.59,[c] −6.41[d]	−6.75[e]
CH$_2$OH	top	−2.42	−2.79	−2.85[a]	−1.98[b]
CHOH	bridge	−3.68	−4.20	−3.68[a]	−3.24[b]
COH	hollow	−5.20	−5.64	−5.25[a]	−4.45[b]
CHO	top	−2.55	−2.80	−2.72[a]	−2.36[b]
CO	hollow	−1.88	−2.34	−1.82[a]	−1.82[b]

[a] Pt$_8$ cluster, B3LYP, from ref 44. [b] PBC, PW91, 1/9 ML, from ref 45. [c] Pt$_8$ cluster, B3LYP, from ref 46. [d] Pt$_{35}$ cluster, B3LYP, from ref 47. [e] PBC, PW91, 1/4 ML, from ref 48.

where the terms on the right-hand side denote the standard-state differences in translational, rotational, and vibrational entropies between the TS and the IS, respectively. The standard-state entropies are given by:[42b]

$$S_{trans} = k_B \left\{ \ln\left[\left(\frac{2\pi m k_B T}{h^2} \right)^{3/2} \frac{k_B T}{P} \right] + \frac{5}{2} \right\} \quad (11)$$

$$S_{rot} = k_B \left\{ \ln\left[\frac{\sqrt{\pi I_A I_B I_C}}{\sigma} \left(\frac{8\pi^2 k_B T}{h^2} \right)^{3/2} \right] + \frac{3}{2} \right\} \quad (12)$$

$$S_{vib} = k_B \sum_i \left(\frac{h\nu_i}{k_B T(e^{h\nu_i/k_B T} - 1)} - \ln(1 - e^{-h\nu_i/k_B T}) \right) \quad (13)$$

where m is the molecular mass, I_A, I_B, and I_C are the principal moments of inertia of the molecule, and σ is the symmetry number. The standard-state pressure $P = 1$ atm was used in the calculation of the standard-state translational entropy of a gas-phase species (CH$_4$) and all standard state quantities were evaluated for $T = 298$ K.

The rate constant in eq 4 can also be written in the form:[41]

$$k = A_o \exp\left(-\frac{E_{act}}{k_B T} \right) \quad (14)$$

In this definition, the preexponential (frequency) factor A_o is also temperature dependent, but the temperature dependence of the exponential term dominates. Equating the corresponding terms of eqs 4 and 14, we have:

$$A_o = \frac{k_B T}{h} \exp\left(\frac{\Delta S^{o\ddagger}}{k_B} \right) \quad (15)$$

$$E_{act} = \Delta H^{o\ddagger} \quad (16)$$

Results and Discussion

The binding energies of all adsorbed intermediates on the Pt$_{10}$ cluster, calculated with both the B3LYP and PW91 functionals, are shown in Table 1. Even though binding energies were not necessary for the prediction of the energy barriers of the reactions, they served to make comparisons of our predictions with other literature results.[44−48] The optimized geometries of the adsorbed species are the initial states of all dehydrogenation reactions and are shown in the uppermost structures of Figures 3−14. In Table 1, the binding energies are compared to those of previously published Pt$_8$ and Pt$_{35}$ cluster/B3LYP

and PBC/PW91 calculations corresponding to 1/4 and 1/9 monolayer (ML) coverage.

As shown in Table 1, this work predicts that methyl (CH$_3$), hydroxymethyl (CH$_2$OH), and formyl (CHO) bind on top sites of the cluster, hydroxyl (OH), methylene (CH$_2$), and hydroxymethylene (CHOH) bind on bridge sites, and methylidyne (CH), carbon (C), hydroxymethylidyne (COH), and carbon monoxide (CO) bind on hollow sites. The cluster surface model cannot differentiate between the two different kinds of hollow sites, fcc and hcp, of the Pt(111) surface. The H atom is predicted to bind on-top but all sites are nearly degenerate. Atomic hydrogen has a nearly flat potential energy profile on the Pt(111) surface. Thus, for H the accepted accuracy limits of DFT methods do not allow a trustworthy comparison with experiment. A minor energetic preference for the on-top site was also found with periodic calculations.[44] The conclusions for the other species also agree with the preferred adsorption sites predicted by periodic boundary condition (PBC) calculations for Pt(111) and other cluster calculations cited in Table 1. The third and fourth columns of Table 1 show that the PW91 functional predicts stronger binding on the Pt$_{10}$ cluster than the B3LYP functional for all adsorbates except H. Literature results with Pt clusters (B3LYP) and periodic boundary conditions (PBC) using the PW91 functional are shown in the last two columns. As representative figures of comparison, we note that the average deviation of our Pt$_{10}$/B3LYP results from the PBC/PW91 results shown in the table is 11%. Our Pt$_{10}$/PW91 results agree less with the PBC/PW91 results, the average deviation being 19%. As expected, our Pt$_{10}$/B3LYP results are in much better agreement with Pt$_8$/B3LYP results, the average deviation being 5%. However, some cluster-size dependence is evident for small clusters, as predicted by comparing the Pt$_8$ and Pt$_{35}$ results cited in column 5 of the table. For the carbon-containing adsorbates that were studied, our results show that the adsorption energy on Pt(111) decreases in the order E(CH) > E(C) > E(COH) > E(CH$_2$) > E(CHOH) > E(CHO) > E(CH$_2$OH) > E(CH$_3$) > E(CO). PBC results predict the same order with the only exception being E(C) > E(CH).

The good agreement of the binding energies of the adsorbates on the Pt10 cluster with those on slabs, obtained by using periodic calculations, manifests that the Pt$_{10}$ cluster is sufficient for studying trends in activation energies of surface reactions that involve the species discussed above. Jacob et al.[49] have shown that a Pt$_{12}$ cluster, which is very similar to the Pt$_{10}$ cluster of our work, does very well in describing top, fcc-hollow, and bridge sites and only fails for hcp-hollow sites. In recent work[47] with Pt$_{35}$ clusters, it was found that none of the CH$_x$ fragments
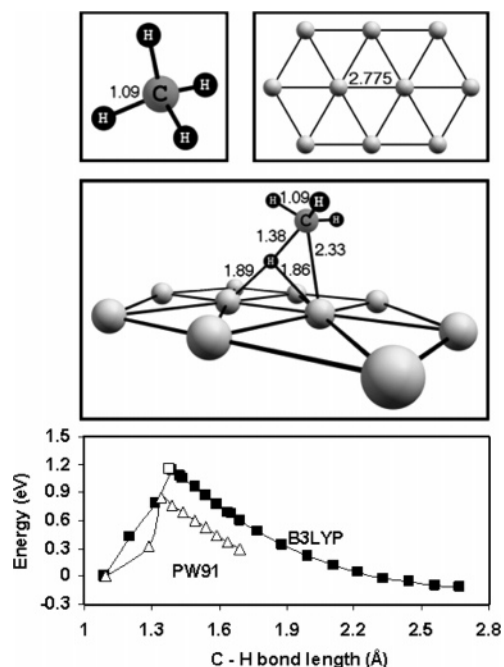
Figure 2. Initial state (top) and transition state (middle) for the reaction $CH_4 \rightarrow {}^*CH_3 + {}^*H$ for the B3LYP functional calculations on a Pt_{10} cluster. Electronic energy profile as a function of C−H bond length (bottom): ■ = B3LYP, ▲ = PW91, □ = transition state (TS) energy for the B3LYP calculation. The zero of energy corresponds to the initial state.

preferred to bind to an hcp site. Of all other adsorbates involved in the mechanism in our work, periodic calculations[45] have shown that none of them prefers the hcp site. Those that bind on 3-fold sites, such as *COH and *CO, are more stable on fcc sites. Furthermore, keeping the cluster fixed does not adversely affect the accuracy because the Pt(111) surface has nearly no relaxation.[47] Jacob and Goddard[47] performed cluster calculations with a 35 atom Pt(111) cluster. The positions of the nonfixed Pt surface atoms changed by less than 3% indicating negligible relaxation.

The initial states and transition states for all reactions that were studied are shown in Figures 2−14 for optimizations with the B3LYP functional. The top picture in each figure is the optimized geometry of the initial state. The second is the optimized geometry of the transition state, followed by the energy profile for the reaction path for B3LYP (■) and PW91 (▲) calculations. The zero of energy corresponds to the initial state for each reaction for both functionals. Open squares (□) refer to TS calculations in which the TS structure was obtained in a separate calculation with direct optimization to the saddle point structure. In every case, there is good agreement between the TS energy and the energy maximum of the reaction coordinate scan. For those cases that a TS calculation did not properly converge or was not attempted, the maximum energy of the reaction coordinate scan provided a good estimate of the TS structure and energy. TS optimizations were not performed for the PW91 functional. For most dehydrogenation reactions, the reaction paths were followed from the initial state to a state just after the TS for hydrogen cleavage, so that the geometry of the final state was not found.

Figure 2 shows the initial state, transition state, and energy profile for the methane dissociative chemisorption reaction $CH_4 \rightarrow {}^*CH_3 + {}^*H$. The initial state consists of the CH_4 molecule and the Pt_{10} cluster at infinite separation. The initial state energy was calculated as the sum of the energies of two separate calculations, in which CH_4 and Pt_{10} are each at their optimum
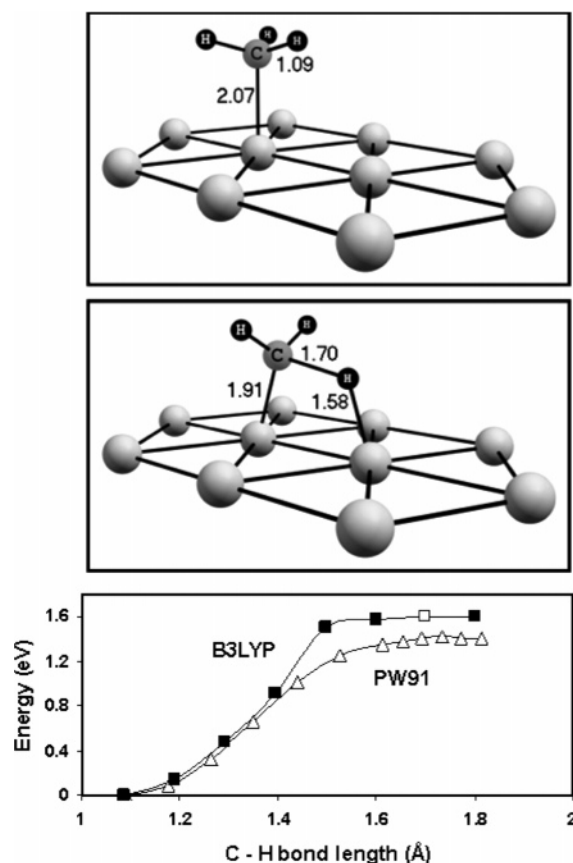

Figure 3. B3LYP initial and transition states for the reaction ${}^*CH_3 \rightarrow {}^*CH_2 + {}^*H$. Energy profile as a function of C−H bond length. □ = B3LYP TS.

spin spate (SM = 1 for CH_4 and SM = 9 for Pt_{10}). The calculated reaction path corresponds to SM = 9. At the TS, the C atom is located 2.33 Å on top of a Pt atom and the H atom 1.38 Å from the C atom and is bridge-bonded to the underlying Pt atoms. The electronic energy barrier predicted by B3LYP is 1.15 eV and that predicted by PW91 is 0.91 eV.

In Figure 2, the energy profile was plotted against the C−H bond length and seems to present a cusp at the TS. This is a consequence of the fact that the actual reaction coordinate is not well represented by the C−H bond length. If the actual reaction coordinate was used instead, the energy profile would be smooth and parabolic around the TS. However, when the TS involves both bond-making and bond-breaking, scanning only one internal coordinate can result in a sudden change in geometry near the TS. This makes the profiles nonparabolic. For example, in Figure 2, the C−H bond length was being decreased at each step to obtain the profile. At the TS, the geometry changed substantially with very small C−H bond length changes, by breaking the Pt−C bond. However, the primary purpose of the energy profiles was to obtain an initial structure for an accurate TS calculation. Thus, the energy profiles presented in these figures use as the independent variable our initial choice of internal variable. After the analytic TS calculation, it was verified by frequency analysis that the TS indeed possessed one imaginary frequency. Similar considerations apply to some of the other reactions in the network.

Figure 3 shows that the preferred adsorption site of methyl (CH_3) is on-top. At the TS geometry for the reaction ${}^*CH_3 \rightarrow {}^*CH_2 + {}^*H$, the C atom has been displaced about 20° from the on-top position toward the bridge-bonded position. The C−H bond length at the TS is 1.70 Å and the dissociating H atom is close to the on-top site of the adjacent Pt atom. The energy
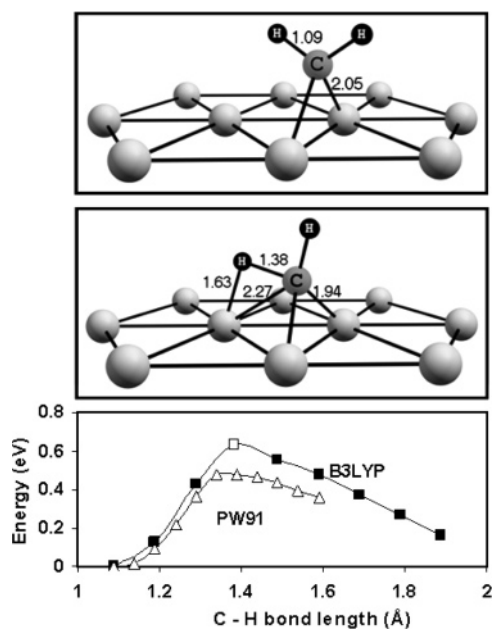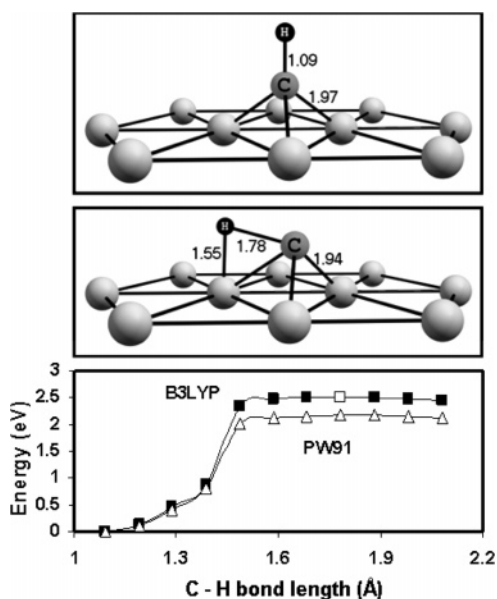
Figure 4. B3LYP initial and transition states for the reaction *CH$_2$ → *CH + *H. Energy profile as a function of C−H bond length. □ = B3LYP TS.

Figure 5. B3LYP initial and transition states for the reaction *CH→ *C + *H. Energy profile as a function of C−H bond length. □ = B3LYP TS.
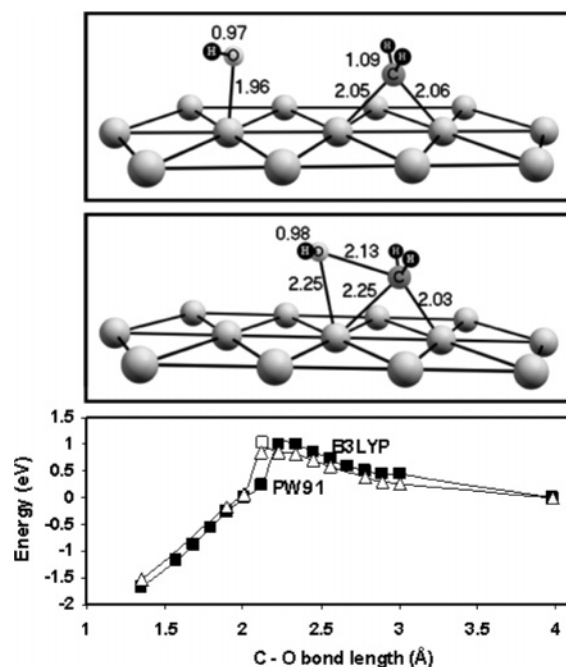

Figure 6. B3LYP initial and transition states for the reaction *CH$_2$ + *OH → *CH$_2$OH on a Pt$_{13}$ cluster. Energy profile as a function of C−O bond length. □ = B3LYP TS.
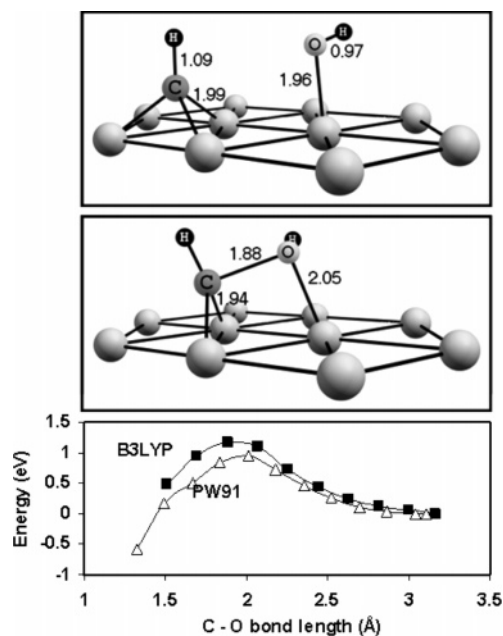

Figure 7. B3LYP initial and transition states for the reaction *CH + *OH → *CHOH. Energy profile as a function of C−O bond length.

barrier predicted by B3LYP for this reaction is 1.61 eV, while PW91 predicts 1.42 eV. The calculated reaction path corresponds to SM = 8.

Figure 4 shows that methylene (CH$_2$) binds at the bridge site. At the TS geometry for the reaction *CH$_2$ → *CH + *H, the C atom has been displaced toward the hollow site, and the dissociating H atom is located 1.38 Å away from the C atom and is close to the on-top site of the adjacent Pt atom. The other H atom has rotated away from the surface. The energy barrier predicted by B3LYP for this reaction is 0.63 eV, while PW91 predicts 0.48 eV. The reaction path was calculated for SM = 7.

Figure 5 shows that methylidyne (CH) binds at the hollow site. At the TS geometry for the reaction *CH → *C + *H, the C atom remains at the hollow site, which is the preferred adsorption site for the final adsorbed C atom. The H atom has

rotated toward one of the Pt binding atoms and is located 1.78 Å away from the C atom. The energy barrier predicted by B3LYP for this C−H cleavage reaction is 2.51 eV, while PW91 predicts 2.18 eV. The reaction path was calculated for SM = 8.

Figure 6 shows the initial and transition states for the reaction *CH$_2$ + *OH → *CH$_2$OH. A Pt$_{13}$ cluster was used for this reaction because on the Pt$_{10}$ cluster *OH shifts to the edge of the cluster upon optimization of the initial state. The on-top adsorbed *OH shown in the top picture of Figure 6 is a local minimum, because B3LYP predicts a small preference (0.15 eV) for the bridge site. Thus a small energy barrier would have to be overcome for *OH to move from a bridge site to the top site that corresponds to the initial state of the reaction. At the
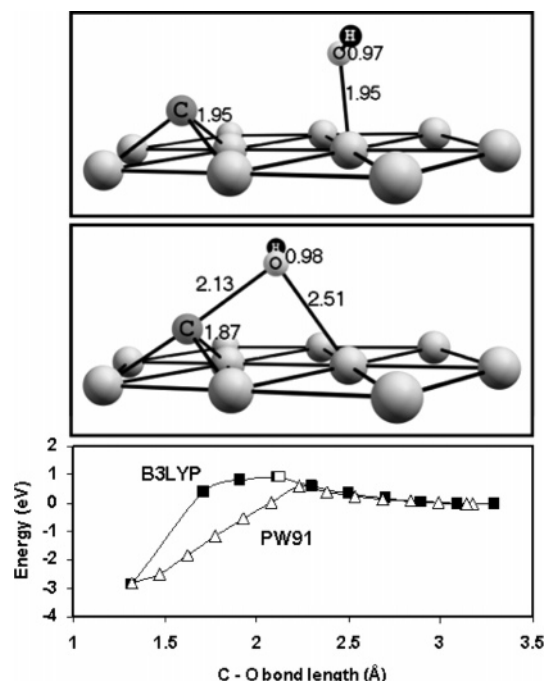
Figure 8. B3LYP initial and transition states for the reaction *C + *OH → *COH. Energy profile as a function of C−O bond length. □ = B3LYP TS.

TS, *OH is located close to on-top of one of the Pt atoms that bind *CH$_2$, while *CH$_2$ has moved closer to the other Pt atom. This Pt atom binds the carbon atom of the product of this reaction, *CH$_2$OH. The energy barrier predicted by B3LYP for this oxygenation reaction is 1.03 eV, whereas PW91 predicts 0.87 eV. The reaction path was calculated for SM = 10 on the 13-atom Pt cluster.

Figure 7 shows the initial and transition states for the reaction *CH + *OH → *CHOH. The initial state consists of *CH bound at the hollow site and *OH bound at the on-top site. At the TS geometry, the C atom has shifted to the bridge position, and the C−O distance is 1.88 Å. The final state is bridge-bonded *CHOH. The energy barrier predicted by B3LYP for this reaction is 1.17 eV, whereas PW91 predicts 0.95 eV. The reaction path was calculated for SM = 7.

Figure 8 shows the initial and transition states for the reaction *C + *OH → *COH. The initial state consists of *C bound at the hollow site and *OH bound at the top site. At the TS geometry, the C atom remains at the hollow site, while *OH has moved toward it. The C−O distance is 2.13 Å at the TS. The final state is *COH bonded though C at the hollow site. The energy barrier predicted by using B3LYP for this reaction is 0.93 eV, while PW91 predicted 0.61 eV. The reaction path was calculated for SM = 8.

Figure 9 shows that hydroxymethyl (CH$_2$OH) binds through C at the top site. At the TS structure for the reaction *CH$_2$OH → *CHOH + *H, the C atom has been displaced about 16° from the on-top position toward the bridge-bonded position. The C−H bond is 1.58 Å and the dissociating H atom has moved toward the on-top site of the adjacent Pt atom. The energy barrier predicted with B3LYP for this reaction is 1.07 eV, while PW91 predicted 0.77 eV. The reaction path was calculated for SM = 8.

Figure 10 shows the initial and transition states for the reaction *CHOH → *COH + *H. The hydroxymethylene (CHOH) group is initially bound at the bridge site. At the TS predicted by B3LYP, the dissociating H atom is 1.76 Å away from the C atom. The C atom is still at the bridge site and
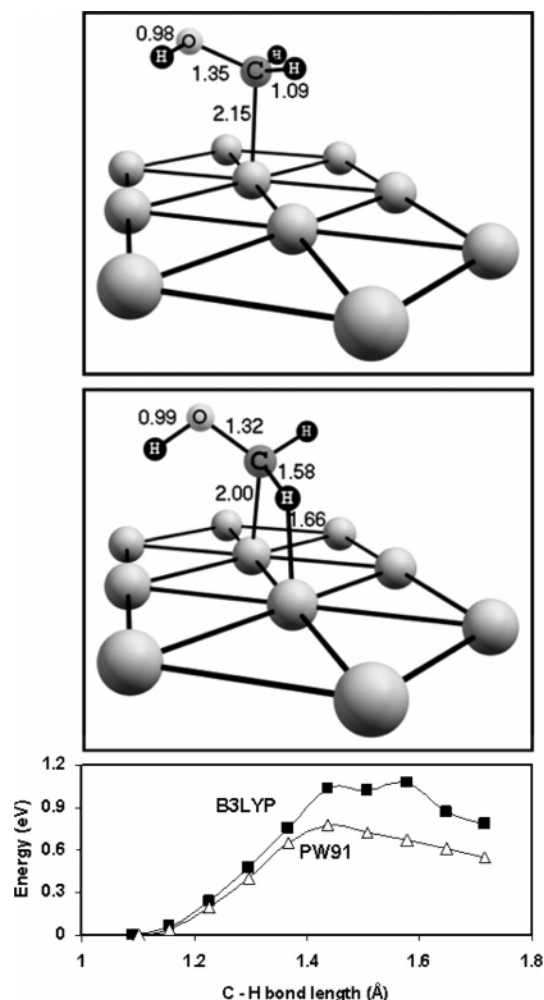

Figure 9. B3LYP initial and transition states for the reaction *CH$_2$OH → *CHOH + *H. Energy profile as a function of C−H bond length.

slightly shifted toward the hollow site, which is its final location. The OH group has rotated away from the surface. The energy barrier predicted with B3LYP for this reaction is 1.33 eV, while PW91 predicted 1.14 eV. The reaction path was calculated for SM = 8.

Figure 11 shows the initial and transition states for the reaction *CHOH → *CHO + *H. For this reaction there is a qualitative difference between the reaction pathways predicted by B3LYP and PW91. The final state for the reaction is predicted by B3LYP to have *CHO bonded on top of one of the Pt atoms that initially bind *CHOH, as shown in the initial state of Figure 13. On the other hand, PW91 predicted a stable state in which *CHO is still bridge bonded, as shown in the first structure of Figure 12. This structure is a local minimum and dissociates to the state *CO + *H + *H with a very small activation energy barrier. For the reaction *CHOH → *CHO + *H, B3LYP predicts a TS in which the C atom is still bridge-bonded and the O−H bond length is 1.50 Å. The energy barrier predicted by B3LYP for this reaction is 0.50 eV, while PW91 predicts 0.35 eV. The reaction path was calculated for SM = 9.

Figure 12 shows the dissociation of the intermediate state of the reaction *CHOH → *CO + *H + *H for the PW91 calculation. The initial state is the final state of the reaction *CHOH → *CHO + *H, as discussed above. Both hydrogen atoms dissociate from this state. At the TS, the Pt−H distance is shown in Figure 12 to be 2.12 Å. This bond length was used as the reaction coordinate for the reaction pathway energy profile. The energy barrier was found to be only 0.08 eV. The
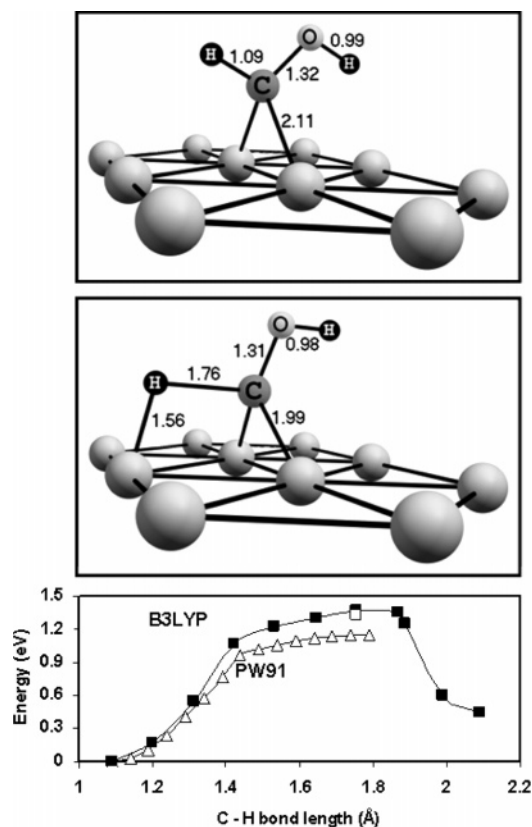
Figure 10. B3LYP initial and transition states for the reaction *CHOH → *COH + *H. Energy profile as a function of C–H bond length. □ = B3LYP TS.
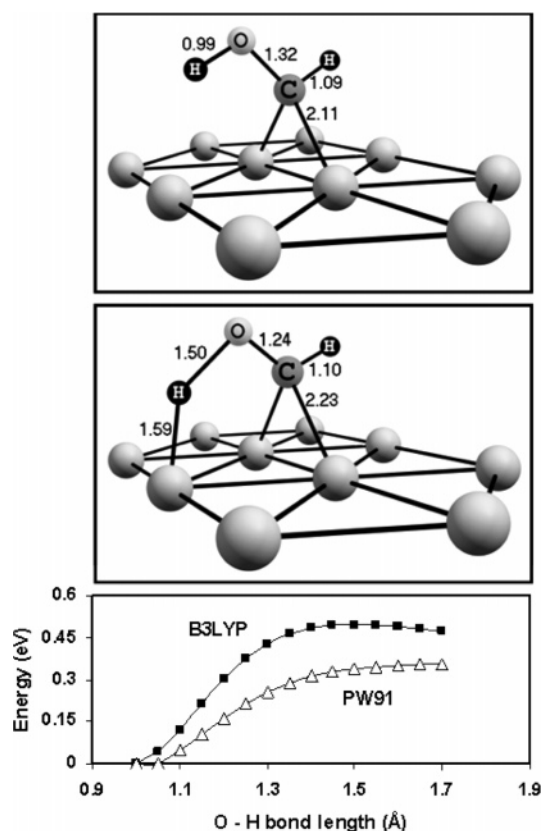
Figure 11. B3LYP initial and transition states for the reaction *CHOH → *CHO + *H. Energy profile as a function of O–H bond length.

reaction path was followed for SM = 9. A previously reported PBC/PW91 study[45] has found that *CHOH dissociates directly
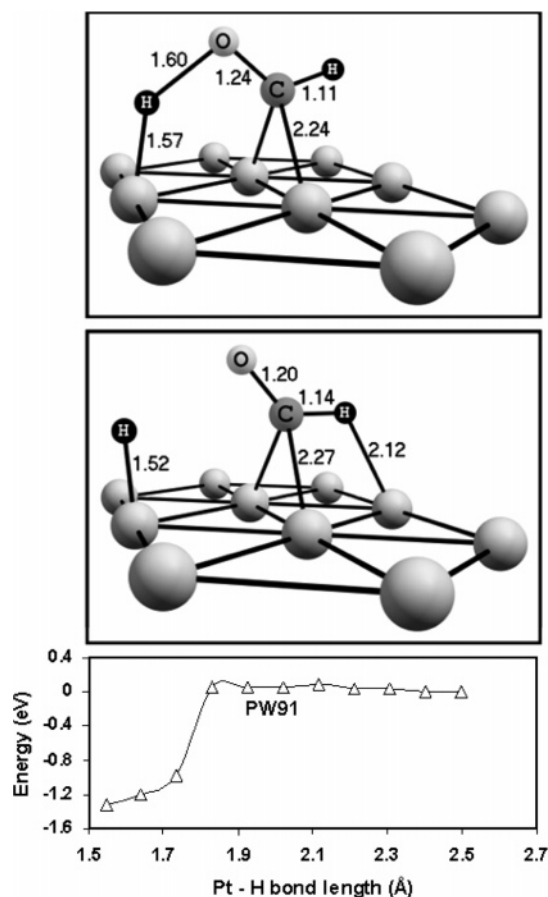

Figure 12. B3LYP initial and transition states for the reaction *CHO → *CO + *H where the initial state is the final state of reaction *CHOH → *CHO + *H. Energy profile as a function of Pt–H bond length.

to the state *CO + *H + *H with a single transition state, after which the dissociation of both hydrogen atoms is spontaneous. Our cluster calculations predict an intermediate local minimum, but the energy barrier of the second step is very small. In effect, the two results are in good agreement.

Figure 13 shows the initial and transition states for the reaction *CHO → *CO + *H, where the initial state is taken to be formyl (CHO) bonded on-top. At the TS for the reaction, the C atom has moved toward the bridge site, the O atom has partly rotated away from the surface, and the C–H bond length is 1.41 Å. The energy barrier predicted by B3LYP for this reaction is 0.76 eV, while PW91 predicts 0.57 eV. However, the reaction pathway described in Figure 12 with the bridge-bonded initial state for *CHO is favorable for the case of the PW91 predictions. The reaction path was calculated for SM = 10.

Figure 14 shows that hydroxymethylidyne (COH) binds at the hollow site with the C–O bond normal to the surface. At the TS structure for the reaction *COH → *CO + *H, the C atom is bridge bonded, the C–O bond rotates toward the surface, and the O–H bond length is 1.32 Å. After dissociation takes place, CO returns to the more stable hollow site. The energy barrier predicted by B3LYP for this reaction is 1.49 eV, while PW91 predicts 1.18 eV. The reaction path was calculated for SM = 8.

Table 2 summarizes the results of the electronic energy calculations for the activation energy barriers (not corrected for ZPE) predicted by B3LYP and PW91 on the Pt_{10} clusters for the reaction pathways of Figure 1. In all cases the energy barriers found with B3LYP were consistently larger than the PW91 ones by 0.15–0.3 eV. The table also shows a characteristic bond
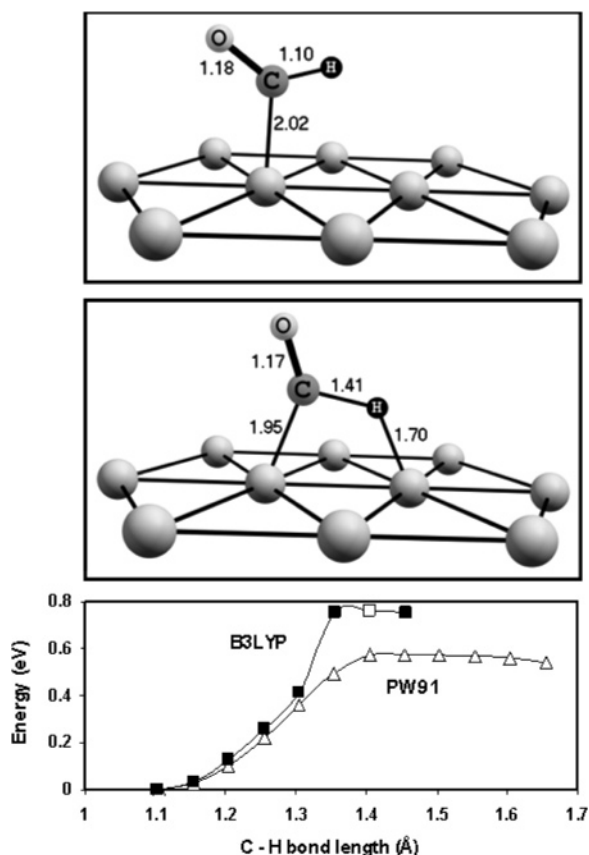
Methane Oxidation Mechanism on Pt(111)

J. Phys. Chem. B, Vol. 110, No. 48, 2006 **24601**

Figure 13. B3LYP initial and transition states for the reaction *CHO → *CO + *H where the initial state is CHO bonded on-top. Energy profile as a function of C–H bond length. □ = B3LYP TS.

length of the TS structure and compares the energy barriers of this work with PBC/PW91 results for those elementary steps that have been previously studied. In one study[50] the activation energies for the reactions *CH$_x$ → *CH$_{x-1}$ + *H were predicted on Pt(111). The electronic energy barriers predicted by our Pt$_{10}$/PW91 model are higher than those predicted by PBC/PW91. However, both methods predict the same order in magnitudes of the energy barriers for this series of reactions. Another PBC/PW91 study[45] predicted the activation energies on Pt(111) for the subnetwork of Figure 1 that involves dehydrogenation reactions of the oxygenated adsorbed radicals. Our Pt$_{10}$/PW91 energy barriers are higher in most cases but again the same order is predicted in their magnitudes. We are not aware of any work that predicted the activation energies of reactions of the type *CH$_x$ + *OH → CH$_x$OH on Pt(111).

Figure 14. B3LYP initial and transition states for the reaction *COH → *CO + *H. Energy profile as a function of O–H bond length. □ = B3LYP TS.

Figure 15 shows schematically the reaction network of Figure 1 and the electronic energy barriers of each reaction for the calculations with the B3LYP functional. In addition to activation energies, preexponential factors are also required to estimate and compare all rate constants using transition-state theory according to eq 14. We performed frequency calculations for the initial and transition states of the reaction network of Figure 1 and estimated preexponential factors using eqs 10–13 and 15 (using T = 298 K). For all elementary surface reactions, except the methane chemisorption step (CH$_4$ → *CH$_3$ + *H), all reactants and products were taken to be immobile and therefore only the vibrational entropy enters into eq 15. Frustrated translation and rotation modes were taken into account[41] in the estimation of the vibrational entropy. We found that preexponential factors for the surface reactions of Figure 1 in which both the initial and final states are adsorbed species vary from 5×10^{11} to 5×10^{13} s^{-1}. This range is in good agreement with PBC literature results[41] for similar reactions on

TABLE 2: DFT-Predicted Electronic Energy Barriers ($\Delta E^{\ddagger}_{elec}$) and Characteristic Bond Length at the Transition State for the Reactions of Figure 1

	$\Delta E^{\ddagger}_{elec}$ (eV)			TS bond length (Å)
reaction	Pt$_{10}$/B3LYP (this work)	Pt$_{10}$/PW91 (this work)	PBC/PW91 (previous work)	(B3LYP) (this work)
CH$_4$ → *CH$_3$ + *H	1.15	0.91	0.63[a]	C–H: 1.38
*CH$_3$ → *CH$_2$ + *H	1.61	1.42	0.88[a]	C–H: 1.70
*CH$_2$ → *CH + *H	0.63	0.48	0.21[a]	C–H: 1.38
*CH → *C + *H	2.51	2.18	1.54[a]	C–H: 1.78
*CH$_2$ + *OH → *CH$_2$OH	1.03	0.87		C–O: 2.13
*CH + *OH → *CHOH	1.17	0.95		C–O: 1.88
*C + *OH → *COH	0.93	0.61		C–O: 2.13
*CH$_2$OH → *CHOH + *H	1.07	0.77	0.63[b]	C–H: 1.58
*CHOH → *COH + *H	1.33	1.14	0.80[b]	C–H: 1.76
*CHOH → *CHO + *H	0.50	0.35	0.43[b]	O–H: 1.50
*COH → *CO + *H	1.49	1.18	0.97[b]	O–H: 1.32
*CHO → *CO + *H	0.76	0.57[c]		C–H: 1.41

[a] From ref 50. [b] From ref 45. [c] Initial state is CHO bonded on top.

$$CH_4 \xrightarrow{1.15\ (1.04)} {}^*CH_3 \xrightarrow{1.61\ (1.43)} {}^*CH_2 \xrightarrow{0.63\ (0.54)} {}^*CH \xrightarrow{2.51\ (2.33)} {}^*C$$

$$\downarrow 1.03\ (1.01) \qquad \downarrow 1.17\ (1.06) \qquad \downarrow 0.93\ (0.91)$$

$${}^*CH_2OH \xrightarrow{1.07\ (0.85)} {}^*CHOH \xrightarrow{1.33\ (1.12)} {}^*COH$$

$$\downarrow 0.50\ (0.34) \qquad \downarrow 1.49\ (1.31)$$
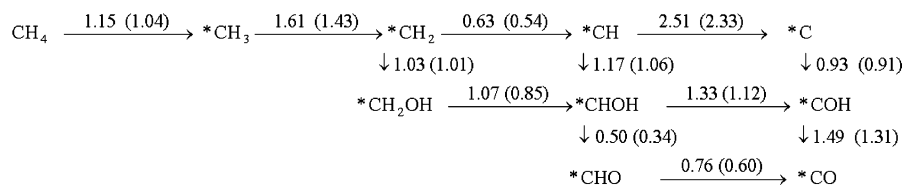
$${}^*CHO \xrightarrow{0.76\ (0.60)} {}^*CO$$

Figure 15. Electronic energy barriers for the reaction network of Figure 1 based on DFT-B3LYP calculations on a Pt_{10} cluster. The values in parentheses were corrected for ZPE.

TABLE 3: Vibrational Frequencies of the Initial and Transition States (IS, TS) of the Reactions $CH_4 \rightarrow {}^*CH_3 + {}^*H$ and ${}^*CH_3 \rightarrow {}^*CH_2 + {}^*H$ on a 10-Atom Pt Cluster at the B3LYP/LANL2DZ/6-31G Level**

reaction	IS frequencies (cm^{-1})	TS frequencies (cm^{-1})
CH4 → *CH3 + *H	3164, 3164, 3164, 3048, 1579, 1579, 1356, 1356, 1356	3264, 3192, 3070, 1524, 1434, 1337, 1096, 1010, 709, 525, 450, 165, 151, 71, −1186
*CH3 → *CH2 + *H	3221, 3212, 3086, 1451, 1447, 1254, 849, 846, 529, 170, 159, 60	3264, 3130, 1945, 1370, 957, 826, 708, 619, 324, 170, 120, −832

TABLE 4: Estimates of Preexponential Factors, Activation Energies, and Rate Constants for the Reactions $CH_4 \rightarrow {}^*CH_3 + {}^*H$ and ${}^*CH_3 \rightarrow {}^*CH_2 + {}^*H$ on Pt (111)

based on current Pt_{10} results	$CH_4 \rightarrow {}^*CH_3 + {}^*H$	${}^*CH_3 \rightarrow {}^*CH_2 + {}^*H$
preexponential factor (298 K)	8.2×10^4 s^{-1} site^{-1} atm^{-1}	1.7×10^{12} s^{-1} site^{-1}
activation energy	99.5 kJ/mol	137.2 kJ/mol
rate constant (298 K)	3×10^{-13} s^{-1} site^{-1} atm^{-1}	1.5×10^{-12} s^{-1} site^{-1}

based on literature PBC results	$CH_4 \rightarrow {}^*CH_3 + {}^*H$	${}^*CH_3 \rightarrow {}^*CH_2 + {}^*H$
activation energy[a]	49.8 kJ/mol	66.9 kJ/mol
rate constant (298 K)	1.5×10^{-4} s^{-1} site^{-1} atm^{-1}	3.1 s^{-1} site^{-1}

[a] From ref 50.

Pt(111). The only exception is the methane chemisorption step that involves translational and rotational entropy losses and has a much smaller preexponential factor, as discussed below. Using eq 14, we calculate that for $T = 298$ K, the difference in activation energies that is required to counterbalance a two orders-of-magnitude difference in preexponential factors is RT $\ln(100) \approx 11.4$ kJ/mol ≈ 0.12 eV. Figure 15 shows that the differences between the electronic energy barriers of elementary reactions that have the same initial state (parallel reactions) are much larger than 0.12 eV. This means that the main reaction pathway can be determined by comparing only the electronic energy barriers of the reactions.

From Figure 15 we conclude that the reaction pathway is $CH_4 \rightarrow {}^*CH_3 \rightarrow {}^*CH_2 \rightarrow {}^*CH \rightarrow {}^*CHOH \rightarrow {}^*CHO \rightarrow CO$. The PW91 calculations predict the same pathway. Furthermore, the rate-limiting step in this pathway can be identified by comparing the rate constant for the methane chemisorption step $(CH_4 \rightarrow {}^*CH_3 + {}^*H)$ with the slowest of the subsequent steps of the reaction pathway. The latter is the one with the highest electronic energy barrier in the reaction pathway, which is the reaction ${}^*CH_3 \rightarrow {}^*CH_2 + {}^*H$. Therefore, we need only perform a quantitative comparison between the rate constants of these two reactions on the Pt_{10} cluster.

The vibrational frequencies corresponding to the initial state and transition states for the two elementary steps $CH_4 \rightarrow {}^*CH_3$ $+ {}^*H$ and ${}^*CH_3 \rightarrow {}^*CH_2 + {}^*H$ are shown in Table 3. They were obtained for the 10-atom Pt cluster by a frequency calculation at the geometry of the corresponding minima and saddle points at the B3LYP/LANL2DZ/6-31G** level. The frequencies include frustrated translation and rotation modes and the negative real part of the imaginary frequency of the TS. On the basis of the discussion in the previous section, for the direct dissociative chemisorption of methane, the reactant has 9 vibrational modes, 3 translational modes, and 3 rotational modes whereas the TS has 14 real positive vibrational modes.

For the surface reaction ${}^*CH_3 \rightarrow {}^*CH_2 + {}^*H$, the reactant has 12 vibrational modes and the TS has 11 real vibrational modes.

The values shown in parentheses in Figure 15 were obtained by applying zero-point energy (ZPE) corrections to the electronic energy barriers. ZPE corrections were obtained with eq 9 by frequency analysis of the intitial and transition states of the reactions. For all dehydrogenation reactions, ZPE corrections act in the direction of decreasing the activation energy barrier by $\sim$0.1−0.2 eV, because C−H and O−H bonds vibrate at higher frequencies than Pt−H bonds. The $CH_x + OH$ reactions are only mildly affected by ZPE. From Figure 15 we can observe that the inclusion of ZPE in the energy barriers does not affect the conclusions on the mechanistic pathway.

Using eqs 5−16 and the results of the electronic energy and frequency calculations, we calculated the preexponential factors, activation energies, and rate constants for the two reactions of interest. The results appear in Table 4. For the direct dissociative chemisorption of methane $(CH_4 \rightarrow {}^*CH_3 + {}^*H)$, in which the reactant is in the gas phase and the TS was considered immobile, the translational partition function of the reactant was evaluated in units of atm^{-1}, in which case the rate constant has units of s^{-1} atm^{-1} site^{-1}, where "site" means free platinum site available for adsorption. For the surface reaction ${}^*CH_3 \rightarrow {}^*CH_2 + {}^*H$, both the reactant and the TS were considered immobile and have no translational degrees of freedom so that the rate constant has units of s^{-1} site^{-1}, where "site" denotes a site covered with a ${}^*CH_3$ species. Molar units have been used for the activation energies in Table 4. The first set of rate constants in the third row of Table 4 was calculated by using the electronic energy barriers calculated with the 10-atom Pt cluster, using the B3LYP functional. The second set of rate constants, in the last row of Table 4, was calculated with the same procedure, using the electronic energy barriers of previous PBC calculations,[50] shown in Table 2, for Pt(111), and using the same preexponential that

Methane Oxidation Mechanism on Pt(111)

J. Phys. Chem. B, Vol. 110, No. 48, 2006 **24603**

we obtained on the 10-atom Pt cluster, since frequency analysis was not performed in the cited work.

The activation energies of the PBC/PW91 calculations are much smaller than the Pt10/B3LYP ones, resulting in rate constants that are many orders of magnitude greater. However, both calculations agree in that the rate constant for CH_4 adsorption is smaller than the rate constant for CH_3 dehydrogenation. Pt10/B3LYP results predict 1 order of magnitude difference between the rate constants, whereas PBC results predict 4 orders of magnitude. Despite the uncertainty in the magnitudes of the rate constants, we can safely conclude that methane chemisorption is the slowest step of the reaction mechanism. This result is a consequence of the combination of both a high electronic energy barrier for dissociative chemisorption caused by Pauli repulsion and the loss of the translational and rotational degrees of freedom upon adsorption of the methane molecule on the surface of the catalyst. The large entropy loss makes the preexponential factor for methane adsorption many orders of magnitude smaller than a surface reaction step. Even though the dissociation of the methyl radical that forms upon adsorption has higher activation energy than CH_4 chemisorption, the entropy effect predominates.

Evident in Table 4 is the sensitivity of the estimates of the rate constants on the DFT estimates of activation energies. This dictates that the nature of the conclusions should be kept strictly qualitative and only used for mechanistic analysis. In a recent experimental kinetic study[19] of methane decomposition on supported platinum catalysts, the activation energy for methane chemisorption was found to be 78 kJ/mol. Our results using a Pt10 cluster were 99.5 (B3LYP functional) and 77 kJ/mol (PW91 functional). The experimental preexponential factor at $T = 873$ K for the same reaction was 2.9×10^6 s^{-1} atm^{-1}. We calculated, using the B3LYP functional, the preexponential factor to be 2.4×10^5 at the same temperature using eq 14 for $T = 873$ K and taking into account the temperature dependence of the preexponential factor. Thus the agreement is satisfactory. The relatively good agreement between the experimental and calculated preexponential factors is evidence that the direct dissociation hypothesis is reasonable. Considering the complexity of the real catalyst, the structure sensitivity of the methane chemisorption process, and simplifications in our approach, this quantitative comparison is somewhat arbitrary. The PBC calculations cited in Table 4 also seem to underpredict the activation energy of methane dissociation. In fact, our results are in better agreement with this experiment than the PBC results. Nevertheless, we limit the implications of our results to strictly qualitative conclusions.

Because the elementary reaction $CH_4 \rightarrow {}^*CH_3 + {}^*H$ was identified as the rate-limiting step in the reaction network of Figure 15, we performed an additional calculation on a 25-atom, 3-layer Pt(111) cluster to investigate the cluster-size effect on the electronic energy barrier. The reaction scan and the geometry that corresponds to the maximum of the scan, and thus approximates the TS structure, are shown in Figure 16. The calculation was performed with the B3LYP functional. The cluster consists of 14 Pt atoms in the first layer, 8 atoms in the second, and 3 atoms in the third layer and all Pt atoms were kept fixed in the optimizations. The reaction scan was calculated for SM = 17. The initial state was taken as the methane molecule and the bare cluster at infinite separation. The approximate TS structure on the Pt25 cluster resembles the structure of the TS on the Pt10 cluster (Figure 2) with small differences in bond lengths. The electronic energy barrier for the dissociative chemisorption of methane on the Pt25 cluster
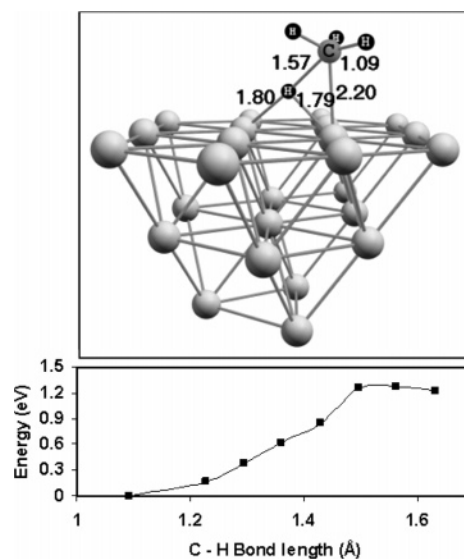

Figure 16. Transition state for the reaction $CH_4 \rightarrow {}^*CH_3 + {}^*H$ on a Pt25 cluster (top) and electronic energy profile as a function of C−H bond length (bottom) calculated with the B3LYP functional.

was calculated to be 1.28 eV. This value is not very different from the energy barrier that was obtained on the Pt10 cluster, 1.15 eV. The comparison suggests only minor cluster-size effects but is not conclusive for this argument. Nevertheless, it helps to establish further confidence for our conclusions on the mechanism of the reation.

The calculations and kinetic analysis in this work assume that the reactions happen at the Pt/vacuum interface. Qualitative arguments can be used to justify that methane chemisorption would be expected to be the rate-determining step at the electrochemical interface as well. Water molecules, OH species, and electrolyte anions are adsorbed at the Pt/electrolyte interface of an acid electrolyte. The strength of the interaction of the catalyst with any of these species is a function of the electrode potential. For a methane molecule to adsorb on the electrode, it has to compete with all molecular species at the double layer. Because methane adsorption requires activation to break the C−H bond, the competition of water and methane for adsorption sites favors water adsorption. Thus, only a fraction of the surface sites would be available for methane to adsorb. Furthermore, the surface charge would tend to increase the binding energy of the more polar water molecules compared to an uncharged surface. Microscopically, a methane molecule can adsorb on a vacant site that is created by the continuous exchange of water molecules between the surface and the solution. Steric hindrance effects and electronic effects caused by electrolyte anions at the interface can also be significant. In a comparative study[27] of methane adsorption on clean and oxygen-precovered Pt(111), it was found that the dissociation probability is smaller on the oxygen-covered surface by 1 to 2 orders of magnitude. An analogous trend can be expected for the electrochemical interface compared to the clean surface. Another factor that would diminish the rate of adsorption from solution is the very low solubility of methane in the electrolyte because the CH_4 dissociation rate increases with increasing the pressure or concentration of CH_4 above the surface.[19] At 25 °C and 1 atm of pressure the solubility of methane in water is[4] 24.4 g of CH_4/10^6 g of H_2O. These considerations suggest that the chemisorption of CH_4 from a liquid electrolyte should be much slower than its chemisorption from the gas phase. This allows us to

extend the conclusion that methane chemisorption is rate limiting in the reaction network of Figure 1 to the electrochemical interface.

The effect of the electrolyte on the decomposition−oxidation pathway may be more complex than its effect on the rate-limiting step. As a first approximation, the electrolyte was not included in our model. In the work of Cao et al.[51] on the mechanism of methanol decomposition, the water phase was found to affect reaction energies. In contrast to our work, Cao et al. did not calculate activation barriers. We note, however, that, despite the fact that including the water phase in the calculations is a considerable improvement in the description of the interface, the agreement of the results of his work with experiment was not good. This can be partly because the electrolyte is not sufficiently represented only with water molecules. It includes protons and electrolyte species as well. Furthermore, static calculations that represent the water phase as a fixed ice-like structrure may be insufficient because they cannot describe the dynamics of the water phase interactions. In this work we have focused on the interactions between the metal and the adsorbed species of the reaction network. The effects of the electrolyte on the mechanism cannot be included realistically in our cluster model.

The effect of the electrode potential was not included in the present calculations. Strictly, the calculations on an uncharged cluster correspond more accurately to the potential of zero charge. Cao et al.[51] performed periodic calculations on the mechanisms of methanol decomposition on Pt and calculated potential-dependent reaction energies. For a wide range of potentials up to 1 V vs NHE, it was found that the magnitude of the electrical potential did not affect the calculated main reaction pathway because the potential had a very similar effect on all reaction energies. This can be expected because all dehydrogenation reactions have a proton in solution in the final state and the potential only has a minor effect on the binding energies of uncharged adsorbed species. Many of these dehydrogenation reactions are common in our work. On the basis of this we do not expect any changes on the rate-determining step and mechanism with varying the potential. It is typical of electrodic reactions that the rate-determining step extends in a wide potential range and this is manifested in single-slope Tafel plots. However, we note that a more realistic model that would be able to make quantitative predictions on the kinetics of methane oxidation would need to account for the effects of both the electrolyte phase and the electrical potential variable.

On the basis of the combination of these results with widely accepted mechanistic aspects of the electrooxidation of CO that forms from organics (i.e., methanol) on platinum[16] we postulate the following complete reaction mechanism for methane electrooxidation at anodic potentials greater that ∼0.4 V. In acid solution, hydroxyl groups form on the surface by deprotonation of water molecules according to the reaction:[16]

$$H_2O \rightarrow {}^*OH + H^+ + e^- \qquad (17)$$
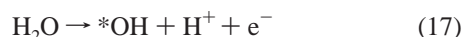
Methane adsorbes dissociatively and the resulting adsorbed H quickly passes into solution at double layer potentials:

$$CH_4 \rightarrow {}^*CH_3 + H^+ + e^- \qquad (18)$$
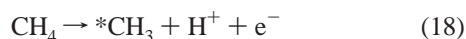
The adsorbed methyl radical forms CO through the pathway $^*CH_3 \rightarrow {}^*CH_2 \rightarrow {}^*CH \rightarrow {}^*CHOH \rightarrow {}^*CHO \rightarrow {}^*CO$, in which all steps are faster than (18). Written consisely:

$$^*CH_3 + {}^*OH \rightarrow {}^*CO + 4H^+ + 4e^- \qquad (19)$$
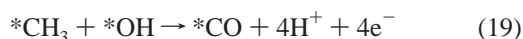
Adsorbed CO is oxidized by adsorbed OH through the reaction:[16]

$$^*CO + {}^*OH \rightarrow CO_2 + H^+ + e^- \qquad (20)$$
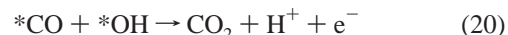
Reactions 7−20 sum up to the complete methane electrooxidation reaction 1. As discussed in the Introduction the experimental results indicate that reactions 17 and 20 proceed faster that (18) at potentials in the double layer region. This means that reaction 18 is the rate-limiting step, which is consistent with the rate-limiting step found in these calculations for Pt-(111). Another implication of this result is that catalysts that remove adsorbed CO more effectively than pure platinum but impede the rate of chemisorption of methane would not increase the rate of methane electrooxidation. This is most probably the case of Pt−Ru alloys that have been found to be less active toward methane electrooxidation compared to pure platinum.[5,10,12,14] For electrode potentials in the hydrogen region (0−0.35 V) no definitive conclusions can be made for the rate-lmiting step, which can be either methane adsorption or *CO oxidation. The above considerations apply to anode potentials greater than ∼0.35 V.

Conclusions and Recommendations

The present computational work has resulted in the following conclusions:

(1) The electrooxidation of methane on Pt proceeds according to the mechanism $CH_4 \rightarrow {}^*CH_3 \rightarrow {}^*CH_2 \rightarrow {}^*CH \rightarrow {}^*CHOH \rightarrow {}^*CHO \rightarrow {}^*CO \rightarrow CO_2$, where the asterisk denotes an adsorbed species.

(2) The rate-determining step for the pathway from CH_4 to *CO is the dissociative chemisorption of CH_4. The rate of this elementary step is slow because it has a relatively large electronic energy barrier and it is accompanied by a large entropic loss. Although not studied here, two further reasons that pertain to liquid electrolytes are the low solubility of methane in water-based electrolytes and the fact that adsorbing methane molecules must compete with water molecules from the solid/liquid interface.

(3) As a result of (2), the only two possible rate-determining steps for the overall reaction of methane electrooxidation are the methane chemisorption step and the *CO oxidation step. This conclusion is in agreement with the experimental observation of no adsorbed organic adlayer at electrode potentials above about 0.4 V at which the *CO oxidation reaction takes place on the Pt surface.

(4) As a result of (2) and (3), an anode catalyst that could possibly result in higher current densities than platinum for the direct oxidation of CH_4 is one for which the rate of adsorption is faster. On the other hand, an improved catalyst should not impede the rates of dehydrogenation and oxidation reactions at the catalyst surface. A catalyst that is able to oxidize adsorbed CO at lower anode potentials would not necessarily enhance the rates of the electrooxidation of methane if it decreases the rate of chemisorption of methane.

(5) The B3LYP exchange-correlation functional predicts significantly higher (by 0.15−0.3 eV) electronic energy barriers than the PW91 functional for the set of reactions that was studied. However, the same trends in the magnitudes of the barriers for different reactions were found. A comparison of the cluster calculations of the present work with PBC calculations available in the literature revealed good agreement in trends but very different results in the magnitudes of electronic energies.

Some recommendations for future work can be identified. On the basis of the above conclusions, quantum mechanical DFT studies of methane adsorption on catalytic surfaces could be used as a screening tool for possible improved catalysts for the electrooxidation process. The results of experimental investigations of methane adsorption at the gas−solid interface of metal catalysts could also prove useful, provided that the catalysts are also stable at the electrochemical environment. Alloys of platinum might offer possibilities for improvement. Furthermore, to our knowledge, the activities of single-crystal surfaces toward the electrooxidation of methane have not been experimentally investigated. Considering the fact that many fuel cell reactions are structure sensitive, as well as the variability of alloy catalysts, the possibility remains open that an effective catalyst for the direct oxidation of methane and other hydrocarbon fuels still evades our knowledge. Ab initio DFT studies at the metal−water interface combined with modeling of electrode potential effects would be expected to provide an improved understanding of the methane electrooxidation process.

References and Notes

(1) Grubb, W. T.; Michalske, C. J. *Nature* (*London*) **1964**, *201*, 287.

(2) Cairns, E. J. *J. Electrochem. Soc.* **1966**, *113*, 1200.

(3) Binder, H.; Kohling, A.; Krupp, H.; Richter, K.; Sandstede, G. *J. Electrochem. Soc.* **1965**, *112*, 355.

(4) Sustersic, M. G.; Cordova O. R.; Triaca, W. E.; Arvia, A. J. *J. Electrochem. Soc.* **1980**, *127*, 1242.

(5) Marvet, R. V.; Petrii, O. A. *Elektrokhimiya* **1967**, *3*, 153.

(6) Hsieh, S. Y.; Chen, K. M. *J. Electrochem. Soc.* **1977**, *124*, 1171.

(7) Niedrach, L. W. *J. Electrochem. Soc.* **1966**, *113*, 645.

(8) Niedrach, L. W.; Tochner, M. *J. Electrochem. Soc.* **1967**, *114*, 17.

(9) Jacquinot, P.; Muller, B.; Wehrli, B.; Hauser, P. C. *Anal. Chim. Acta* **2001**, *432*, 1.

(10) Berthelot, S.; Gehain, E.; Hahn, F.; Leger, J. M.; Srinivasan, S.; Lamy, C. Extended Abstracts, Electrochemical Society Meeting, Boston, 1998; Vol. 98-2, Abstract 1090.

(11) Bockris, J.O'M; Srinivasan, S. *Fuel Cells*: *Their Electrochemistry*; McGraw-Hill: New York, 1969; p 158.

(12) Cairns, E. J. In *Advances in Electrochemistry and Electrochemical Engineering*; Delahay, P., Tobias, C. W., Eds.; John Wiley: New York, 1971; Vol. 8, p 337.

(13) Taylor, A. H.; Brummer, S. B. *J. Phys. Chem.* **1968**, *72*, 2856.

(14) Hahn, F.; Melendres, C. A. *Electrochim. Acta* **2001**, *46*, 3525.

(15) Markovic, N. M.; Ross, P. N. *CatTech* **2000**, *4*, 110.

(16) Leger, J.-M. *J. Appl. Electrochem.* **2001**, *31*, 767.

(17) Bagotzky, V. S.; Vassiliev, Y. B.; Khazova, O. A. *J. Electroanal. Chem.* **1977**, *81*, 229.

(18) Larsen, J. H.; Chorkendorff, I. *Surf. Sci. Rep.* **1999**, *35*, 163.

(19) Wei, J.; Iglesia, E. *J. Phys. Chem. B* **2004**, *108*, 4094.

(20) Luntz, A. C.; Harris, ? *Surf. Sci.* **1991**, *258*, 397.

(21) Walker, A. V.; King, D. A. *Phys. Rev. Lett.* **1999**, *82*, 5156.

(22) Luntz, A.; Bethune, D. S. *J. Chem. Phys.* **1989**, *90*, 1274.

(23) McMaster, M. C.; Madix, R. J. *J. Chem. Phys.* **1993**, *98*, 9963.

(24) Gee, A. T.; Hayden, B. E.; Mormiche, C.; Kleyn, A. W.; Riedmüller, B. *J. Chem. Phys.* **2003**, *118*, 3335.

(25) Fuhrmann, T.; Kinne, M.; Tränkenschuh, B.; Papp, C.; Zhu, F. J.; Denecke, R.; Steinrück, H.-P. *New J. Phys.* **2005**, *7*, 107.

(26) Seets, D. C.; Wheeler, M. C.; Mullins, C. B. *J. Chem. Phys.* **1997**, *107*, 3986.

(27) Valden, M.; Xiang, N.; Pere, J.; Pessa, M. *Appl. Surf. Sci.* **1996**, *99*, 83.

(28) Schoofs, G. R.; Arumainagam, C. R.; McMaster, M. C.; Madix, R. *J. Surf. Sci.* **1989**, *215*, 1.

(29) Bukoski, A.; Abbott, H. L.; Harrison, I. *J. Chem. Phys.* **2005**, *123*, 094707.

(30) Ukraintsev, V. A.; Harrison, I. *J. Chem. Phys.* **1994**, *101*, 1564.

(31) Luntz, A. C.; Winters, H. F. *J. Chem. Phys.* **1994**, *101*, 10980.

(32) Gross, A.; Wilke, S.; Scheffler, M. *Phys. Rev. Lett.* **1995**, *75*, 2718.

(33) Koper M. T. M. In *Modern Aspects of Electrochemistry*; Vayenas, C. G., Conway, B. E., White R. E., Eds.; Kluwer Academic/Plenum: New York, 2003; No. 36, pp 51−130.

(34) Feibelman P. J.; Hammer, B.; Nørskov, J. K.; Wagner, F.; Scheffler, M.; Stumpf, R.; Watwe, R.; Dumesic. *J. Phys. Chem. B* **2001**, *105*, 4018.

(35) Frisch, M. J.; Trucks, G. W.; Schlegel, H. B.; Scuseria, G. E.; Robb, M. A.; Cheeseman, J. R.; Montgomery, J. A., Jr.; Vreven, T.; Kudin, K. N.; Burant, J. C.; Millam, J. M.; Iyengar, S. S.; Tomasi, J.; Barone, V.; Mennucci, B.; Cossi, M.; Scalmani, G.; Rega, N.; Petersson, G. A.; Nakatsuji, H.; Hada, M.; Ehara, M.; Toyota, K.; Fukuda, R.; Hasegawa, J.; Ishida, M.; Nakajima, T.; Honda, Y.; Kitao, O.; Nakai, H.; Klene, M.; Li, X.; Knox, J. E.; Hratchian, H. P.; Cross, J. B.; Bakken, V.; Adamo, C.; Jaramillo, J.; Gomperts, R.; Stratmann, R. E.; Yazyev, O.; Austin, A. J.; Cammi, R.; Pomelli, C.; Ochterski, J. W.; Ayala, P. Y.; Morokuma, K.; Voth, G. A.; Salvador, P.; Dannenberg, J. J.; Zakrzewski, V. G.; Dapprich, S.; Daniels, A. D.; Strain, M. C.; Farkas, O.; Malick, D. K.; Rabuck, A. D.; Raghavachari, K.; Foresman, J. B.; Ortiz, J. V.; Cui, Q.; Baboul, A. G.; Clifford, S.; Cioslowski, J.; Stefanov, B. B.; Liu, G.; Liashenko, A.; Piskorz, P.; Komaromi, I.; Martin, R. L.; Fox, D. J.; Keith, T.; Al-Laham, M. A.; Peng, C. Y.; Nanayakkara, A.; Challacombe, M.; Gill, P. M. W.; Johnson, B.; Chen, W.; Wong, M. W.; Gonzalez, C.; Pople, J. A. *Gaussian 03*, Revision C.02; Gaussian, Inc.: Wallingford, CT, 2004.

(36) Becke, A. D. *J. Chem. Phys.* **1993**, *98*, 5648.

(37) Perdew, J. P.; Chevary, J. A.; Vosko, S. H.; Jackson, K. A.; Pederson, M. R.; Singh, D. J.; Fiolhais, C. *Phys. Rev. B*: *Condens. Matter* **1992**, *46*, 6671.

(38) Hay P. J.; Wadt, W. R. *J. Chem. Phys.* **1985**, *82*, 270.

(39) Herzberg, G. *Molecular Spectra and Molecular Structure*; Vol. 3, Electronic Spectra and Electronic Structure of Polyatomic Molecules; D. Van Nostrand: New York, 1966.

(40) Kua, J.; Goddard, W. A., III *J. Phys. Chem. B* **1998**, *102*, 9481.

(41) Gokhale, A. A.; Kandoi, S.; Greeley, J. P.; Mavrikakis, M.; Dumesic, J. A. *Chem. Eng. Sci.* **2004**, *59*, 4679.

(42) Cramer, C. J. *Essentials of Computational Chemistry*, 2nd ed.; John Wiley: Chichester, UK, 2004; (a) p 527 and (b) pp 355−366.

(43) Chorkendorff, I.; Niemantsverdiet, J. W. *Concepts of Modern Catalysis and Kinetics*; Wiley- VCH Verlag: Weinheim, Germany, 2003; p 121.

(44) Kua, J.; Goddard, W. A., III *J. Am. Chem. Soc.* **1999**, *121*, 10928.

(45) Greeley, J.; Mavrikakis, M. *J. Am. Chem. Soc.* **2004**, *126*, 3910.

(46) Kua, J.; Goddard, W. A., III *J. Phys. Chem. B* **1998**, *102*, 9492.

(47) Jacob, T.; Goddard, W. A., III *J. Phys. Chem. B* **2005**, *109*, 297.

(48) Ford, D. C.; Xu, Y.; Mavrikakis, M. *Surf. Sci.* **2005**, *587*, 159.

(49) Jacob, T.; Muller, R. P.; Goddard, W. A., III *J. Phys. Chem. B* **2003**, *107*, 9465.

(50) Michaelides, A.; Liu, Z.-P.; Zhang, C. J.; Alavi A.; King D. A.; Hu P. *J. Am. Chem. Soc.* **2003**, *125*, 3704.

(51) Cao, D.; Lu, G.-Q.; Wieckowski, A.; Wasileski, S. A.; Neurock, M. *J. Phys. Chem. B* **2005**, *109*, 11622.